

Charge density wave induced nodal lines in LaTe_3

Received: 28 November 2022

Accepted: 30 May 2023

Published online: 19 June 2023

 Check for updates

Shuvam Sarkar¹, Joydipto Bhattacharya^{2,3}, Pampa Sadhukhan¹, Davide Curcio⁴, Rajeev Dutt^{2,3}, Vipin Kumar Singh¹, Marco Bianchi⁴, Arnab Pariari⁵, Shubhankar Roy⁶, Prabhat Mandal⁵, Tanmoy Das⁷, Philip Hofmann⁴, Aparna Chakrabarti^{2,3} & Sudipta Roy Barman¹✉

LaTe_3 is a non-centrosymmetric material with time reversal symmetry, where the charge density wave is hosted by the Te bilayers. Here, we show that LaTe_3 hosts a Kramers nodal line—a twofold degenerate nodal line connecting time reversal-invariant momenta. We use angle-resolved photoemission spectroscopy, density functional theory with an experimentally reported modulated structure, effective band structures calculated by band unfolding, and symmetry arguments to reveal the Kramers nodal line. Furthermore, calculations confirm that the nodal line imposes gapless crossings between the bilayer-split charge density wave-induced shadow bands and the main bands. In excellent agreement with the calculations, spectroscopic data confirm the presence of the Kramers nodal line and show that the crossings traverse the Fermi level. Furthermore, spinless nodal lines—completely gapped out by spin-orbit coupling—are formed by the linear crossings of the shadow and main bands with a high Fermi velocity.

Recent years have witnessed rapid development in the understanding of the physics of cooperative charge density wave (CDW) electronic state^{1–12}. In particular, the interplay of the CDW electronic state with the non-trivial topological phases provides an interesting platform for the discovery of novel quasiparticles such as, axion insulator^{3,13}, quantum spin-Hall insulator¹⁴, fractional Chern insulator states¹⁵ and manipulation of topologically protected states^{16,17}. CDW can drive topological phase transitions by modifying the symmetry of the lattice, such as breaking the inversion symmetry¹⁸. Interesting topological phases are frequently found in non-centrosymmetric materials, such as nodal chain fermions¹⁹, Dirac and Weyl fermions^{20–22}, hourglass fermions protected by glide reflection²³, Kramers Weyl semimetal (KWS)²⁴ and recently predicted Kramers nodal line (KNL) metal²⁵. KNLs differ from the Weyl nodal lines because they join two time reversal invariant momenta (TRIM) points and should appear in all achiral non-

centrosymmetric time reversal symmetry (TRS) preserving systems²⁵. For the subclass of nonsymmorphic symmetry, KNLs emerge from the Γ points. Unlike the previously known nodal lines manifested by band inversion²⁶, the KNLs are robust under spin-orbit coupling (SOC) unless the protecting lattice symmetries such as TRS, mirror, or roto-inversion symmetries are broken. KNL fermions have been predicted to exhibit physical properties such as quantized optical conductivity²⁵. However, in this emerging field, to the best of our knowledge, the experimental evidence of KNL is limited to the work by Shang et al.²⁷ who reported that transition metal ruthenium silicides belong to this class and exhibit unconventional superconductivity based on muon spin spectroscopy and density functional theory (DFT).

In recent years, multiple fascinating findings in LaTe_3 ^{1,4,7,28–30}—a member of the RTe_3 (R represents a rare earth element) family with highest CDW transition temperature of 670 K^{31,32}—have rekindled the

¹UGC-DAE Consortium for Scientific Research, Khandwa Road, Indore 452001, Madhya Pradesh, India. ²Theory and Simulations Laboratory, Raja Ramanna Centre for Advanced Technology, Indore 452013, Madhya Pradesh, India. ³Homi Bhabha National Institute, Training School Complex, Anushakti Nagar, Mumbai 400094, Maharashtra, India. ⁴Department of Physics and Astronomy, Interdisciplinary Nanoscience Center (INANO), Aarhus University, Aarhus C 8000, Denmark. ⁵Saha Institute of Nuclear Physics, HBNI, 1/AF Bidhannagar, Kolkata 700064, India. ⁶Vidyasagar Metropolitan College, 39, Sankar Ghosh Lane, Kolkata 700006, India. ⁷Department of Physics, Indian Institute of Science, Bangalore 560012, India. ✉e-mail: barmansr@gmail.com

scientific interest of the community in this TRS preserving material. The detection of an axial Higgs boson mode in LaTe_3 from Raman spectroscopy has been related to unconventional CDW excitation¹. Photoinduced CDW state with topological defects in this material has been discovered from ultrafast electron diffraction and related studies^{7,28}. The non-centrosymmetry in LaTe_3 was established from the structure determined by single crystal x-ray crystallography³³ as well as from the appearance of the B_1 symmetric Raman modes³⁴. Transport studies have revealed that LaTe_3 possesses an unusually high non-saturated longitudinal magnetoresistance³⁰, which is similar to that of nodal line material³⁵. In addition, LaTe_3 possesses very high carrier mobility³⁰, which, in conjunction with its high transition temperature, makes it a promising contender for next-generation electronics. Only a few angle resolved photoemission spectroscopy (ARPES) measurements on LaTe_3 have been reported in the literature^{7,36}. Using time resolved ARPES, Zong et al.⁷ examined light-induced melting of the CDW state of LaTe_3 . A previous research by Brouet et al.³⁶ demonstrated that the CDW-induced shadow bands hybridize with the main bands existing in the non-CDW state creating a CDW gap along a particular direction of the Brillouin zone (BZ). Theoretical calculation of the electronic susceptibility as well as experiments have shown that q dependent electron-phonon coupling plays an important role in stabilizing the CDW state in RTe_3 ^{37–39}. A recent DFT study on a free-standing monolayer of LaTe_3 revealed that tensile strain would increase the CDW order, while compressive strain would suppress it, and superconductivity could develop³⁷. In light of the fact that LaTe_3 is a non-centrosymmetric achiral material with TRS intact, topological phases brought on by inversion symmetry breaking in conjunction with other symmetries may be anticipated in the CDW state.

Here, from an in-depth study of the band structure of LaTe_3 single crystal in the CDW state by combining ARPES and ab-initio DFT using realistic experiment-based structure, we establish the existence of a KNL in a CDW material. It originates from the interaction of the shadow band and the main band, and is hosted by the TRS and the lattice symmetries. Furthermore, spinless nodal lines that are entirely gapped out by SOC are also identified.

Results

Modulated structure of LaTe_3 in the CDW state

The CDW in LaTe_3 has been reported to be unidirectional with an incommensurate wave vector \mathbf{q}_{CDW} of $0.2757(4)\mathbf{c}^*$ from x-ray crystallography³³, where \mathbf{c}^* is the reciprocal lattice vector along k_z in the non-CDW state. It may be noted that an incommensurate structure can be represented as commensurate with a large unit cell such that its \mathbf{q}_{CDW} is equal to the incommensurate value within the experimental accuracy of x-ray crystallography^{40,41}. So, after considering different possible combinations of the numerator and the denominator of a fraction that could represent \mathbf{q}_{CDW} , we arrive at a 29-fold (29f) structure ($1 \times 1 \times 29$) derived from the experimental structure (see Methods) with $\mathbf{q}_{\text{CDW}} = \frac{8}{29}\mathbf{c}^* = 0.2759\mathbf{c}^*$ that matches experimental $0.2757(4)\mathbf{c}^*$ within its experimental accuracy. It has 232 atoms in the unit cell with positions almost coinciding with those given by x-ray crystallography [230 atoms have zero (0.0000 Å) displacement with respect to ref. 33, while only 2 atoms show a displacement of 0.0001 Å]. It should be mentioned that inorganic materials with such large unit cells do exist in nature^{42–44}. The 29f structure has a non-centrosymmetric space group of $C2cm$ (SG #40) that is the basic space group reported in ref. 33.

The 29f structure is unique because, although being commensurate, it represents the incommensurate structure of LaTe_3 within the experimental accuracy^{40,41}. However, because of the large size of the unit cell, DFT calculations become computationally challenging and expensive. So, we consider a relatively smaller unit cell with 56 atoms (Fig. 1a) that has 7-fold (7f) modulated structure ($1 \times 1 \times 7$) with $\mathbf{q}_{\text{CDW}} = \frac{2}{7}\mathbf{c}^* = 0.2857\mathbf{c}^*$ with same symmetry as the 29f structure. Figure 1a shows that LaTe_3 is made up of two main structural units: the Te2-Te3 bilayer

that hosts the CDW and the La-Te1 corrugated slab. The Te bilayer, highlighted by blue double-sided arrows, is weakly coupled by van der Waals interaction. The primitive unit cell of the 29f structure is shown in Supplementary Fig. 1. Supplementary Fig. 2a, b shows the displacement of the Te atoms in the CDW state for both 7f and 29f structures with respect to the non-CDW positions. By comparing with the atom positions from the structure (.cif) file of ref. 33, we show that the atom positions are indistinguishable in the 29f structure. The 7f structure shows rather small deviations in both \mathbf{q}_{CDW} (3.5%) and the amplitude of modulation (5%). In Supplementary Fig. 3, we show how the non-centrosymmetry arises in LaTe_3 by breaking the M_x mirror symmetry. Also, the orientation of the polar axis along x is indicated, which is dictated by the retained M_z mirror and \tilde{M}_y glide symmetries.

The signature of the CDW in the Te layer has been directly observed from our high resolution scanning tunneling microscopy (STM) topography image in Fig. 1b. The white solid lines show the distorted Te net formed by connecting the Te atoms (orange circles). Also, the white dashed lines showing the average positions of the adjacent Te chains are not equidistant. These observations from STM show that the M_x mirror symmetry is broken, which results in non-centrosymmetry. \mathbf{q}_{CDW} has been estimated from the satellite spots observed in the Fourier transform of the STM image as well as from the low energy electron diffraction (LEED) pattern that also shows CDW related satellite spots (circled in Fig. 1c) besides the (1×1) spots; see Supplementary Note 1 and Supplementary Fig. 4. The non-centrosymmetry in the CDW state of LaTe_3 is also demonstrated by the peaks of B_1 symmetry mode³⁴ in the Raman spectrum in Supplementary Fig. 5.

The high symmetry directions are shown in the BZ of the 7f structure in Fig. 1d inscribed within the non-CDW BZ. Since the BZ is related to the ordering of the lattice constants of the conventional cell, its comparison with the primitive unit cell is shown in Supplementary Fig. 6a, b. In our notation, the horizontal plane in the BZ is represented by k_x - k_z and \mathbf{q}_{CDW} is oriented along k_z . The CDW BZ, containing features such as the primitive reciprocal lattice vectors and all the pertinent high symmetry points and directions as well as their coordinates, is depicted in Supplementary Fig. 6c. In what follows, we present the ARPES data in the next subsection that is subsequently compared with the effective band structure based on the 7f structure. The DFT bands for the 7f structure without (w/o) SOC are discussed next, followed by the band structure with SOC. The existence of the KNL is established and ARPES bands along the high symmetry directions are discussed in the last two subsections. Finally, in the Discussion section, we confirm the existence of the KNL and the spinless nodal line for the 29f structure.

Crossing of the bilayer-split shadow and main bands from ARPES

An $E(k_z)$ ARPES intensity plot in a generic direction parallel to ΓZ at $k_x = 0.68 \text{ \AA}^{-1}$ i.e., near the X point (the length of ΓX being 0.737 \AA^{-1}) is shown in Fig. 2a in the CDW state (see Methods for the experimental details). The direction of the ARPES measurement is shown by the red line denoted by a in Fig. 2g. Figure 2a shows two main bands (inner and outer) centered around X that cross E_F at $k_z = \pm 0.15$ and $\pm 0.21 \text{ \AA}^{-1}$, respectively. The outer main band disperses down to binding energy (E) of about 1.25 eV, while the inner band has a nearly flat bottom at -0.8 eV. It is interesting to note that a relatively weaker band centered around $k_z = \pm 0.41 \text{ \AA}^{-1}$ is a replica of the main band shifted by \mathbf{q}_{CDW} ($= 0.28\mathbf{c}^* = 0.41 \text{ \AA}^{-1}$), as shown by two horizontal white dashed arrows. This replica band crosses E_F at $k_z = 0.21$ and 0.61 \AA^{-1} and disperses down to $E - 1.25$ eV. No shift in its position along E compared to the main band is observed, which indicates that it is related to the initial state CDW superlattice⁴⁵. It has been referred to in the literature as the shadow band^{36,45,46}. The signature of the shadow band is also evident in the Fermi surface shown in Fig. 1e, where shadow Fermi surface branches appear at a separation of \mathbf{q}_{CDW} from the main branches, as shown by black dashed arrows in the metallic region around the X point parallel to the ΓZ direction. In the Supplementary Note 2, a

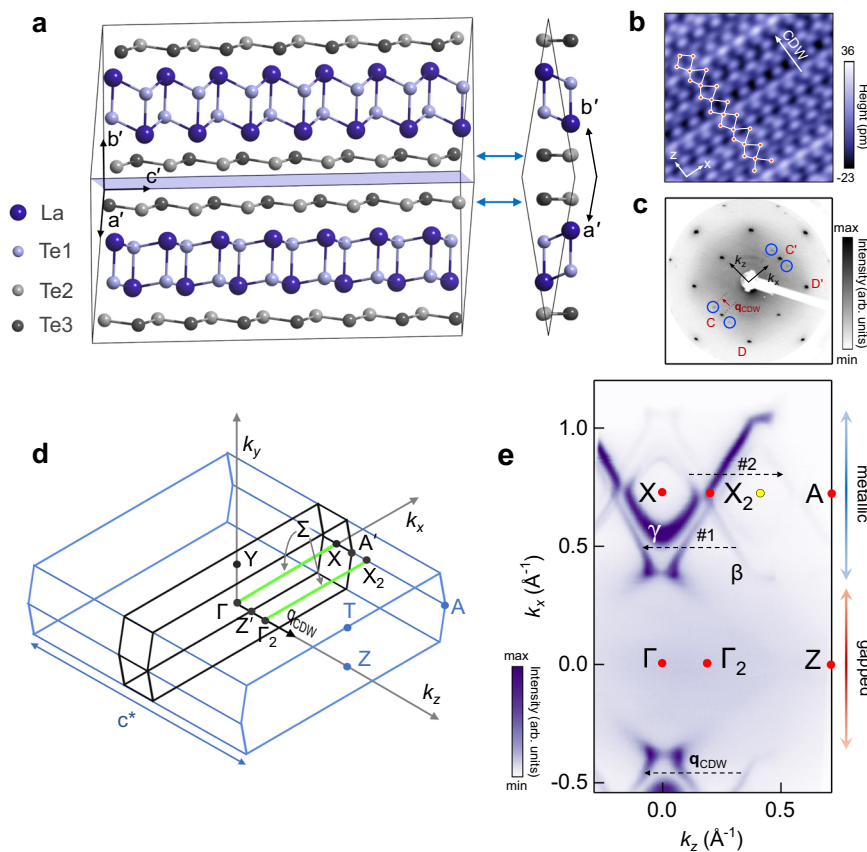


Fig. 1 | Structure, Brillouin zone and the Fermi surface of LaTe₃ in the CDW state. **a** The 7-fold ($1 \times 1 \times 7$) modulated primitive unit cell of LaTe₃ comprising of 56 atoms with wave vector $\mathbf{q}_{\text{CDW}} = \frac{2}{7}\mathbf{c}'$ viewed perpendicular (left) and parallel (right) to the \mathbf{c}' direction. The lattice constants are $a' = b' = 13.256 \text{ \AA}$, $c' = 30.778 \text{ \AA}$ with $\alpha = \beta = 90^\circ$, and $\gamma = 160.99^\circ$. The cleavage plane (light blue) occurs in between the two weakly interacting Te layers indicated by the blue double-sided arrows. **b** High resolution scanning tunneling microscopy topography image ($4.2 \text{ nm} \times 4.2 \text{ nm}$) obtained with bias voltage of 0.2 V and a tunneling current of 0.4 nA . The overlaid orange circles represent the Te atom positions. The white dashed lines show the average positions of the adjacent Te chains. **c** Low energy electron diffraction pattern, measured with

77 eV primary beam energy, shows the reciprocal space in the k_x - k_z plane (black arrows). C, D, C', and D' represent the main spots; the CDW satellite spots are highlighted by blue circles. **d** The CDW Brillouin zone (BZ) (black) is shown within that of the non-CDW state (light blue). The high symmetry points⁸³ are indicated in these respective colors. Γ , Y and X points coincide for both. The Σ lines represented by ΓX and $\Gamma_2 X_2$ in the 2nd BZ are shown in green color. See Supplementary Fig. 6c for the other high symmetry points and directions in the CDW BZ. **e** The Fermi surface in the CDW state measured by ARPES, where the length of the black dashed arrows (#1, #2) that join the shadow branches with the main branches of the Fermi surface represents \mathbf{q}_{CDW} . The colorbar shows the intensity in arbitrary units (arb. units).

discussion about the Fermi surface and \mathbf{q}_{CDW} obtained from the average separation of the shadow and main branches is provided. $\mathbf{q}_{\text{CDW}} = 0.28 \pm 0.005\mathbf{c}'$ determined in this way agrees with the values obtained from STM and LEED (see Supplementary Note 1), as well as that from transmission electron microscopy ($\mathbf{q}_{\text{CDW}} = 0.28 \pm 0.01\mathbf{c}'$)⁴⁷. However, the accuracy of these approaches for calculating \mathbf{q}_{CDW} is substantially worse compared to x-ray crystallography³³.

In Fig. 2a, the shadow and the main bands resemble an inverted V and meet each other close to E_F at $k_z = \pm 0.21 \text{ \AA}^{-1}$ (highlighted by a green dashed oval). This region is shown in an expanded scale as a curvature plot in Fig. 2e, where the red and black dashed lines suggest a possible crossing of nearly linear bands at E_F . The Fermi velocities of these bands, determined using the expression $(\frac{1}{\hbar} \frac{dE}{dk_z})$, turn out to be $(1.2 \pm 0.05) \times 10^6$ and $(1 \pm 0.05) \times 10^6$ m/s for the shadow and main bands, respectively. These values are comparable to graphene (1×10^6 m/s⁴⁸), indicating large mobility of LaTe₃ in agreement with recent report from Hall conductivity measurements³⁰.

To further probe these bands and their possible crossing, ARPES was performed over a range of k_x out of which three representative plots (along the red lines parallel to a up to d in Fig. 2g) are shown in Fig. 2b–d. Interestingly, as k_x decreases, both the main and the shadow bands spread out in k_z and the crossings—highlighted by green dashed ovals—shift below E_F to larger E . However, note that their k_z position

remains unchanged around $X_2 \approx \pm \frac{1}{2}\mathbf{q}_{\text{CDW}}$. In Fig. 2b–d, splitting in both the shadow and the main bands are observed. This is also observed in Fig. 2e, as shown by the double-sided red arrows. This is dubbed as bilayer splitting and has been reported in other RTe₃ members^{36,49,50}, bilayer graphene⁵¹, and cuprate superconductors⁵². In Supplementary Note 3, from the decrease in the bilayer splitting calculated by DFT as the separation of the Te bilayers increases, we confirm that it is related to the coupling between the two adjacent Te layers. Moreover, it is observed for both non-CDW and CDW states of LaTe₃ and does not appear in LaTe₂ that has a single layer of Te but exhibits CDW^{53,54}. These results indicate that the bilayer splitting would occur in a Te bilayer independent of the CDW.

Both the bilayer-split shadow bands—denoted by su (sd) for smaller (larger) E , see Fig. 2f—are shifted by \mathbf{q}_{CDW} from the corresponding main bands denoted by mu and md . This is shown by the white dashed horizontal arrows in Fig. 2a, b. This leads to formation of four crossings between the main and the shadow bands, as shown in Fig. 2f. A stack of k_z - k_x isosurface plots with E varying from 0 to 0.6 eV with the crossings visible at $E = 0.5 \text{ eV}$ (a zoomed curvature plot shown) and a stack of momentum distribution curves (MDCs) taken near the crossings in Fig. 2c are shown in Supplementary Fig. 13a, b.

The crossings are denoted by left (L , highlighted by blue rectangle, crossing of mu and sd i.e., $mu \otimes sd$), right (R , orange rectangle,

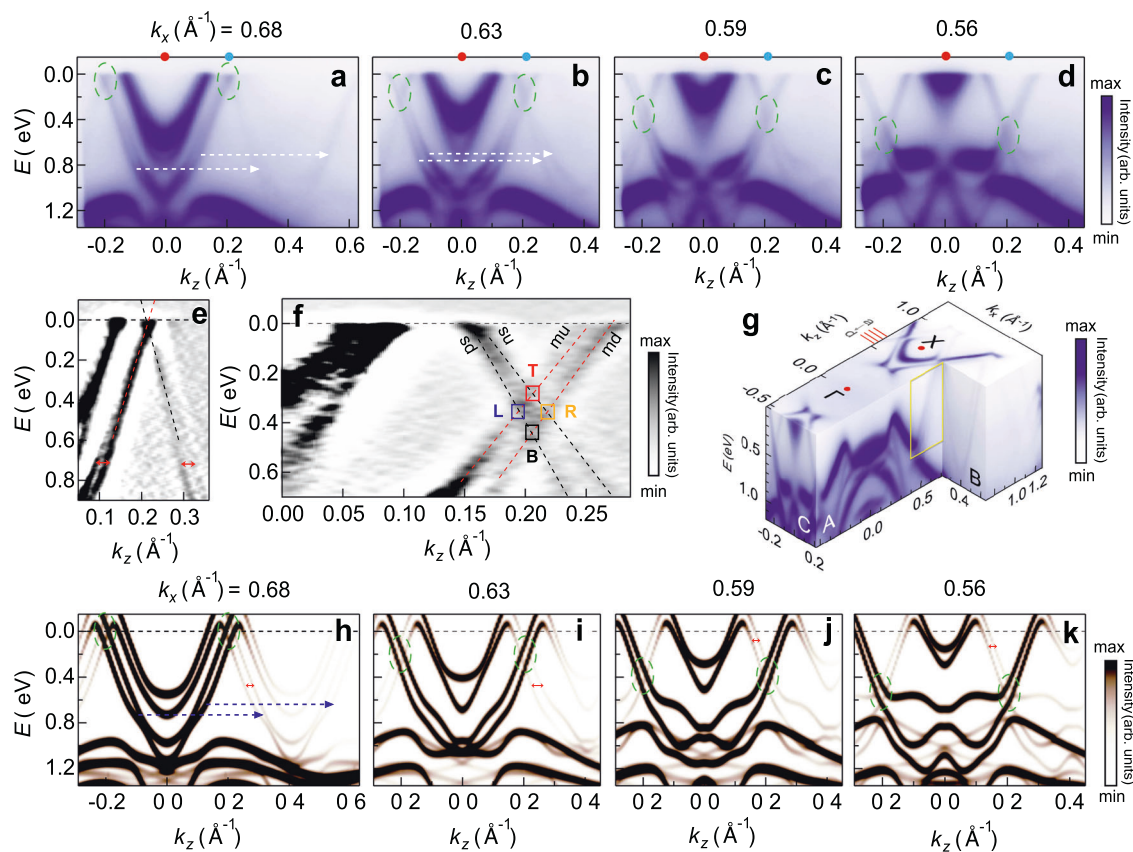


Fig. 2 | Crossings between the bilayer-split shadow and the main bands. $E(k_z)$ ARPES intensity plots measured at 100 K for $k_x =$ **a** 0.68, **b** 0.63, **c** 0.59, and **d** 0.56 \AA^{-1} . The red and blue dots at the top of the panels indicate the k_z positions of the ΓX and $\Gamma_2 X_2$ high symmetry lines. The white dashed arrows in panels **a** and **b** represent the \mathbf{q}_{CDW} and the band crossing regions are highlighted by green dashed ovals. $E = 0$ represents the E_F . These panels share same y axis and colorbar, the latter is shown on the right of panel **d**. **e** A zoomed view of the near E_F region of panel **a** around $k_z = 0.21 \text{\AA}^{-1}$, the dashed red (black) line that represents the main (shadow) band is obtained by curve fitting (see Methods). The double-sided red arrows show the bilayer splitting. **f** Curvature plot of a part of panel **c** shown in an expanded scale: the *L*, *B*, *R* and *T* crossings are highlighted by blue, black, yellow and red rectangles, respectively. The *T* and *B* crossings occur on the $\Gamma_2 X_2$ line. The dashed red [black]

lines representing the bilayer split main (*mu*, *md*) [shadow (*su*, *sd*)] bands are obtained by curve fitting as in **e**, **f**. **g** Cut *A* at $k_z = 0.216 \text{\AA}^{-1}$ of an E - k_z - k_x ARPES intensity plot shows the dispersion of the *R* crossing and the *mu* and *sd* bands within the yellow rectangle. A shadow band is observed in the cut *B*. The ARPES cuts measured along the red lines *a*-*d* on the k_x axis are shown in panels **a**-**d**. **h**-**k** The effective band structure (EBS) along k_z obtained by band unfolding at similar k_x values as in **a**-**d**, respectively. The intensity scale represents the spectral weights calculated from band unfolding and the size of the dots is related to the instrumental resolution. **h**-**k** share same y axis and colorbar, the latter is shown on the right of **k**. The double-sided red arrows indicate the bilayer splitting and the blue arrows in panel **h** represent the \mathbf{q}_{CDW} . The band crossing regions are highlighted by green dashed ovals.

$md \otimes su$), top (*T*, red rectangle, $mu \otimes su$), and bottom (*B*, black rectangle, $md \otimes sd$) (Fig. 2f). While Fig. 2a-d shows the band dispersion at discrete k_x values, we show a continuous dispersion of the *R* crossing in cut *A* of Fig. 2g. Here, the $E(k_x)$ at $k_z = 0.216 \text{\AA}^{-1}$ shows the loci of the *R* crossing within the yellow rectangle.

ARPES with different photon energies shows negligible k_y dependence of the crossings. For example at $k_x = 0.58 \text{\AA}^{-1}$, Supplementary Fig. 14a-d shows that their position (highlighted by green dashed ovals) remains almost unchanged with k_y . This is summarized in Supplementary Fig. 14e through a k_y - k_z map at $E = 0.39 \text{ eV}$, where the two crossings at $k_z = \pm 0.2 \text{\AA}^{-1}$ (marked by yellow arrows) show almost no change with k_y , indicating the quasi-2D nature of LaTe_3 .

Effective band structure from DFT compared to ARPES

Multiple crossings indicated by ARPES is a surprising result since hybridization gap is generally expected at the band touching points between the Bloch states connected by \mathbf{q}_{CDW} ^{50,55}. The $E(k_z)$ bands calculated for the 7f structure at different k_x as in the experiment are shown in an extended zone scheme spread over the non-CDW BZ in Supplementary Fig. 15. Many bands are observed in the CDW state due to band folding. Their complexity hides the influence of the CDW on the electronic bands and impedes their interpretation and direct

comparison with ARPES. So, an effective band structure (EBS) has been calculated by unfolding the bands in the non-CDW BZ⁵⁶⁻⁵⁸. In Fig. 2h-k, EBS shows the distribution of states as a function of their energy and momenta with appropriate spectral weight, where broadening similar to the experiment has been applied. Variations in the spectral weight is evident resulting in dissimilar EBS in the different CDW BZs.

The importance of the EBS calculation is that despite the CDW effect being small with the modulation amplitude being only $\sim 4.5\%$ of the average Te2-Te3 distances, the EBS reveals the shadow bands. These are shifted from the main bands by \mathbf{q}_{CDW} (blue dashed arrows) in excellent agreement with ARPES (compare Fig. 2h-k with Fig. 2a-d). In contrast, the bands in the non-CDW state, where obviously the CDW amplitude is zero, shows only the main bands (Supplementary Fig. 16a). An analysis of the orbital character establishes that the shadow bands (as well as the main bands) are of predominantly in-plane Te p_x - p_z character, see the Supplementary Fig. 17a-f. The out-of-plane p_y character becomes slightly significant only for $E > 0.6 \text{ eV}$, and the contributions from the La-Te1 block is negligible. However, transfer of electrons from La to the Te net determines the band filling in the Te2-Te3 layer and this has been calculated using the Bader charge analysis (see Supplementary Note 4 including Supplementary Table 1 and refs. 59-61).

From Fig. 2h, we find that the outer branch of the shadow band disperses towards E_F and crosses the main band around $k_z = \pm 0.21 \text{ \AA}^{-1}$ (highlighted by a dashed green oval). The inner branch of the shadow band which disperses to about 0.6 eV, although more prominent in the EBS, has its counterpart in experiment in the curvature plot shown in Supplementary Fig. 16b. A bunch of bands that disperse weakly between 1.15 to 1.6 eV is observed in both theory and experiment at similar E . In Fig. 2i–k, for progressively smaller k_x values, the EBSs portray the crossings (L , R , T and B) at similar E - k_z as observed in ARPES (compare Fig. 2i–k with Fig. 2b–d). The observation of four distinct crossings is related to the bilayer splitting that is also observed in the EBS (horizontal red double arrows in Fig. 2h–k). Also note that the bilayer splitting (Δk_z) increases with E for the different k_x and this trend is observed in both experiment and theory (see Supplementary Table 2). Similar variation of Δk_z has been recently reported for NdTe_3 ⁶². The agreement of ARPES and EBS is also good at larger E : the main bands around 0.8 eV become flatter and move to lower E . Important to note is that from ARPES the crossings appear to be gapless (Fig. 2a–f) within the experimental and lifetime broadening. Although this is supported by the EBS (Fig. 2h–k), note that the calculations have been performed here with a k step size (δk_z) of $6 \times 10^{-3} \text{ \AA}^{-1}$, and the broadening is comparable to ARPES, both of which might conceal potential presence of minigaps. In the subsequent subsections, we show the DFT bands calculated with smaller δk_z to further probe the nature of the crossings.

Spinless nodal lines formed by the L and R crossings

The $E(k_z)$ bands from DFT with small δk_z ($= 5 \times 10^{-4} \text{ \AA}^{-1}$) w/o SOC show that the L and R crossings are gapless (Fig. 3a). This is reconfirmed in Fig. 3b, c by the bands calculated with even smaller δk_z ($= 1 \times 10^{-5} \text{ \AA}^{-1}$). It

is interesting to note that these crossings occur at generic points of the BZ in the k_x - k_z plane and the bands involved are linear (Fig. 3a–c). The unfolded EBS in Supplementary Fig. 18 shows nice agreement with the ARPES intensity plots in Fig. 2c, f and demonstrate the linearity of the bands around L and R . The velocities calculated from their slopes are similar to that obtained at E_F from Fig. 2e. Although these bands originate from the in-plane p orbitals with small difference in contributions from the p_x and p_z orbitals as shown in Supplementary Fig. 17a–f, md and sd bands belong to M_1 irreducible band representation (irrep), while mu and su belong to M_2 irrep. Thus both L and R crossings are formed by bands belonging to different irreps (Fig. 3a–c). Note that band folding results in two more relatively flat bands in Fig. 3a, i (also shown in Supplementary Fig. 18a, c where these are indicated by red arrows). These bands are not detected in the unfolded EBS because of their reduced spectral weight (Supplementary Fig. 18b, d) and are also not observed in ARPES (Fig. 2c, f).

The crossings disperse with k_x and at larger $k_x = 0.685 \text{ \AA}^{-1}$ compared to 0.59 \AA^{-1} , L and R crossings traverse the E_F (Supplementary Fig. 19a–c). In fact, calculations for a series of k_x values establish that the gapless linear crossings occur over an extended range of the E - k space (Supplementary Fig. 20). The loci of each crossing form a continuous curve in the momentum space that has been referred to as a nodal line. A direct comparison of the (E, k_x) cuts from ARPES (Fig. 3f, g for R and L , respectively) shows that the positions of both the nodal lines are in excellent agreement with DFT. Both disperse between $(E, k_x) = (0 \text{ eV}, -0.7 \text{ \AA}^{-1})$ to $(-0.6 \text{ eV}, -0.5 \text{ \AA}^{-1})$ with k_z at 0.195 and 0.22 \AA^{-1} for L and R , respectively. Thus, the crossings appear within an energy window of $E - 0.6 \text{ eV}$ to the E_F . Their projections in the k_x - k_z plane form a pair of approximately parallel nodal lines that are 0.2 \AA^{-1} in length and appear at a separation of $k_z - 0.02 \text{ \AA}^{-1}$ in a general direction on this

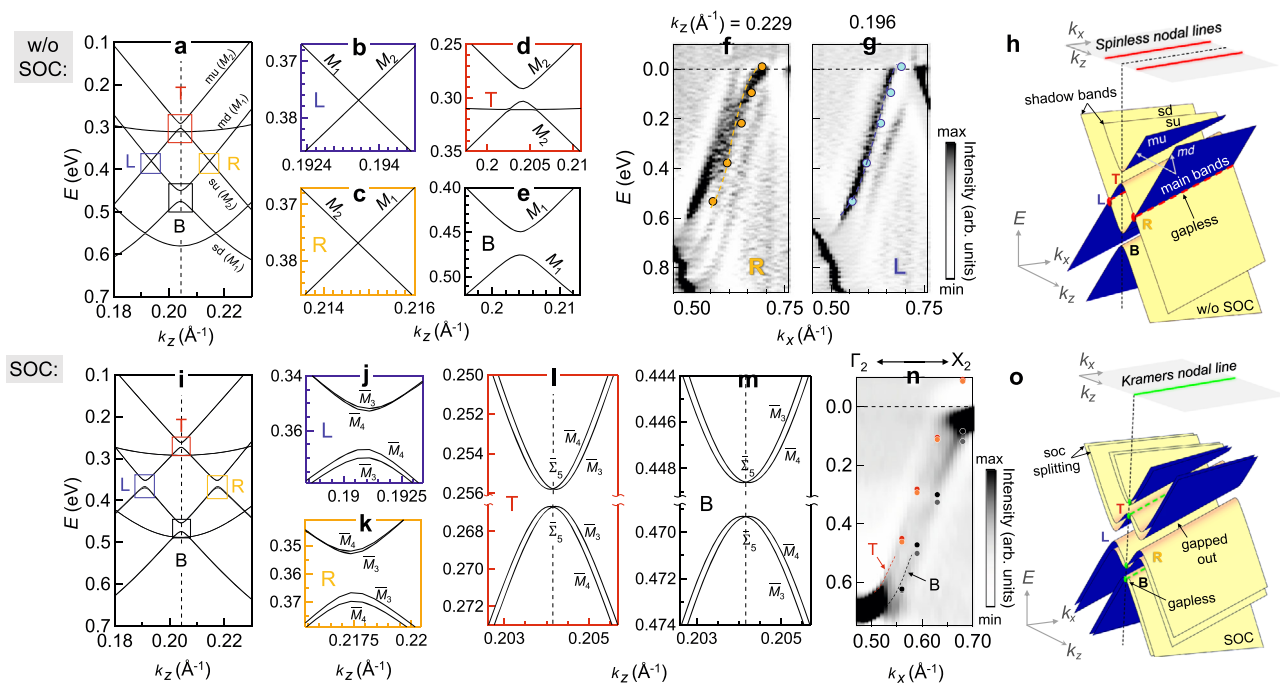


Fig. 3 | Band crossings and the Kramers nodal line (KNL). **a** $E(k_z)$ bands at $k_x = 0.59 \text{ \AA}^{-1}$ without (w/o) spin-orbit coupling (SOC) for the 7f structure. The irreducible representations are shown. The vertical dashed line represents the k_z point on $\Gamma_2 X_2$ i.e., the Σ line in the 2nd BZ (see Fig. 1d). Zoomed colored rectangles of a show the bands around **b** L , **c** R , **d** T , and **e** B . Comparison of ARPES and DFT for **f** R at $k_z = 0.229 \text{ \AA}^{-1}$ and **g** L at $k_z = 0.196 \text{ \AA}^{-1}$. The positions of these crossings obtained from DFT (orange and blue filled circles for R and L , respectively) are superimposed. The dashed orange and blue curves serve as guide to the eye. **h** A schematic representation of the gapless L and R crossings in the E - k_z - k_x space (red

dashed lines) and their projection on the k_x - k_z plane showing the spinless nodal lines (thick red lines on both sides of the Σ line). **i–m** Same as **a–e** except that the calculations are performed with SOC. **n** $E(k_x)$ ARPES intensity plot at $k_z = 0.204 \text{ \AA}^{-1}$ (dashed red and black curves serve as guide to the eye) compared with the positions of the crossings from DFT for T (red, light red circles) and B (black, gray circles). **o** A schematic representation of the four crossings (green dashed lines) related to the upper and lower branches of T and B . The KNL appears along the Σ line and is denoted by a green thick line on the k_x - k_z plane.

plane (red solid lines in Fig. 3h). These appear parallel to but on either sides of Γ_2X_2 that occurs at $k_z = 0.204 \text{ \AA}^{-1}$. These nodal lines are formed by two fold crossings of nondegenerate bands in the absence of spin and so are referred to as spinless nodal lines. The existence of these nodal lines is shown for the 29f structure of LaTe₃ in the Discussion section.

With inclusion of SOC, it is intriguing to find that both the L and R crossings (and hence the nodal lines) are entirely gapped out by minigaps of 14 meV (for $k_x = 0.59 \text{ \AA}^{-1}$) to 17 meV (for $k_x = 0.685 \text{ \AA}^{-1}$) into upper and lower branches, as shown in Fig. 3i–k and Supplementary Fig. 19g, h. A schematic is shown in Fig. 3o. The gap is formed by hybridization of bands belonging to same one dimensional double group irrep involving both \overline{M}_3 and \overline{M}_4 .

Note that non-centrosymmetry should lift the SU(2) spin degeneracy. This is visible through the spin splitting of both the upper and lower branches in Fig. 3j, k. These spin-split bands belong to different irreps \overline{M}_3 and \overline{M}_4 and do not cross each other. The splittings for both L and R are k -dependent, it is maximum at the extrema (~ 3 meV for lower and 1 meV for the upper branch) and decreases away from it.

Evidence of Kramers nodal line from the T and B crossings

In the case of T and B crossings, the shadow and main bands belong to the same irrep, leading to hybridization-related minigaps w/o SOC and the creation of upper and lower branches (Fig. 3a, d, e). The inclusion of SOC provides a fascinating outcome: the spin-split bands in both the upper and lower branches of T and B exhibit gapless crossings (Fig. 3l, m), which contrasts the bands at L and R (Fig. 3j, k). Each branch of T and B crosses at the same $k_z = 0.204 \text{ \AA}^{-1}$ (dashed lines in Fig. 3i, l, m) resulting in four crossings. This value of k_z is special, since it falls on the Γ_2X_2 line of the CDW BZ (i.e., ΓX or the Σ line) (Fig. 1d). At $k_x = 0.59 \text{ \AA}^{-1}$, the four crossings appear at different E : 0.256 (0.267) eV for the upper (lower) branch of T , and 0.448 (0.469) eV for upper (lower) branches of B .

These gapless crossings are observed over a range of k_x , as in the case of L and R . For example, at $k_x = 0.685 \text{ \AA}^{-1}$, the crossings disperse to smaller E and in this case both the branches of T (B) are above (below) the E_F (Supplementary Fig. 19f, i, j). Significantly, the crossings always appear at same k_z , i.e., along the Σ line, suggesting that the crossings may be enforced by the lattice symmetries along this direction.

The band irreps with SOC shown in Fig. 3l, m are as follows: the crossing belongs to a double valued irrep that is two dimensional ($\overline{\Sigma}_5$), while away from it, the spin-split bands have one dimensional (\overline{M}_3 or \overline{M}_4) representation. Significantly, the Σ line that emerges from the Γ point has the little group that is isomorphic to C_{2v} point group and has symmetries such as the two fold rotation about the k_x -axis denoted by C_{2x} : $\{2_{100}|0, 0, 0\}$, glide reflection perpendicular to the y axis in the k_x - k_z plane followed by a translation of $\frac{1}{2}c$ given by \overline{M}_y : $\{m_{010}|0, 0, \frac{1}{2}\}$ and an off-centered mirror perpendicular to the k_z axis M_z : $\{m_{001}|0, 0, \frac{1}{2}\}$. Γ is a TRIM point, where according to the Kramers theorem, each band is at least doubly degenerate. The little group of Σ is related to that of Γ by the compatibility relations. We find that Γ and Σ are represented by two dimensional double-valued irreps: $\overline{\Gamma}_5$ and $\overline{\Sigma}_5$, respectively. These representations are similar, as shown in Supplementary Table 3⁶³. The Σ line passes through the X point with coordinates (0.257, 0.257, 0) and meets the TRIM point Y_2 (0.5, 0.5, 0) in the next BZ (see Supplementary Fig. 21). Y_2 also belongs to double-valued two dimensional irrep \overline{Y}_{25} that is same as Γ and Σ (Supplementary Table 3). The condition that at the TRIM points the representations should be time reversal invariant is satisfied since both $\overline{\Gamma}_5$ and \overline{Y}_{25} are pseudo-real⁶³. Thus, $\overline{\Gamma}_5 \cdot \overline{\Sigma}_5 \cdot \overline{Y}_{25}$ is able to support two fold degeneracy of the bands along ΓXY_2 i.e., the Σ line. This is a Kramers nodal line (KNL) that occurs along the Σ line in the mirror-invariant k -plane in the presence of TRS, and the additional rotational symmetry constrains the KNL along a high symmetry direction²⁵. Xie et al.²⁵ have proved the existence of KNL along the C_2 rotational axis ($\{2_{100}|0, 0, 0\}$), which in our case is along k_x that lies in

the k_x - k_y mirror plane ($\{m_{001}|0, 0, \frac{1}{2}\}$). In Fig. 3o, the projection of the loci of the crossings of the four pairs of bands in the E - k_z - k_x space on the k_x - k_z plane shows the KNL (thick green line) that enforces the crossings.

The bands in a plane that cuts the KNL perpendicularly—as is the case in Fig. 3i—have been described in the literature as two-dimensional massless Dirac Hamiltonian with the Berry curvature concentrated at the crossing²⁵. These authors demonstrated that the Berry phase around a KNL is quantized as $m\pi \text{ mod } 2\pi$. In case of quadratic and cubic dispersion of these bands, the crossing has been dubbed as a higher-order Dirac point²⁵. In the present case, both the upper and lower branches of T and B exhibit quadratic dispersion close to the crossings, as is evident in Fig. 3l, m. Consequently, the gapless crossings in LaTe₃ that are associated with the KNL are higher-order Dirac points. The gapless crossings and their quadratic dispersion are demonstrated for the 29f structure of LaTe₃ in the Discussion section.

ARPES and DFT along the KNL and other directions

In Fig. 4a, the bands calculated along the KNL (i.e., ΓX) show two pairs of degenerate bands related to the T and B crossings, highlighted by green shading, and zoomed in the insets *i, ii*. The ARPES intensity plot in Fig. 3n represents these bands. These are also identified by the degenerate crossings of bands in the $E(k_z)$ direction enforced by the KNL (Fig. 3l, m). The existence of the KNL between 0.5 and 0.7 \AA^{-1} along k_x is affirmed by ARPES through an excellent agreement of the positions of the crossings obtained from DFT (filled circles) that are overlaid on the experimental data in Fig. 3n. The agreement is also evident in the Supplementary Fig. 22, where Fig. 3i is superposed on Fig. 2f. However, the energy separations between the upper and lower branches of both T and B are too small to be resolved by ARPES. Similarly, the quadratic nature visible in a tiny k_z range shown in Fig. 3l, m is not distinguished, see the regions enclosed by the red and black rectangles in Supplementary Fig. 22. Nonetheless, ARPES is consistent with DFT, and both show that the crossings disperse from $E = 0.6$ eV at $k_x = 0.55 \text{ \AA}^{-1}$ and traverse the E_F at $k_x = 0.65$ – 0.7 \AA^{-1} .

We find that every band along ΓX is degenerate due to the double degeneracy enforced by the KNL (see for example the insets *i–v* of Fig. 4a) and belong to two dimensional $\overline{\Sigma}_5$ irrep. Besides the T and B related bands discussed above, there are other bands that cross E_F in Fig. 4a. These bands—numbered as 1, 2, and 3 and highlighted by orange shading—have not been observed in the ARPES along Γ_2X_2 ($k_z = 0.204 \text{ \AA}^{-1}$) due to their low spectral weight at this k_z . However, these three bands are clearly visible in the ARPES intensity plot along ΓX ($k_z = 0 \text{ \AA}^{-1}$) in Fig. 4b and disperse across the E_F in splendid agreement with the EBS along the same direction in Fig. 4c. At larger E other bands (numbered as 4–12) in the EBS along ΓX are in very good agreement with ARPES (Fig. 4b). On the other hand, the bands around the T and B crossings both along and perpendicular to the KNL have negligible spectral weight around ΓX and so are observed neither in EBS nor ARPES in Fig. 4b, c. However, the band structure shows the crossings formed by band folding in every BZ, see Supplementary Fig. 15, where the crossing region is highlighted by red ovals. This shows the importance of performing ARPES over multiple CDW BZs in the direction of \mathbf{q}_{CDW} to decipher the influence of the CDW on the electronic band structure.

Perpendicular to the KNL along ΓZ (Λ), the bands are represented by one dimensional irreps (Supplementary Fig. 21 and Supplementary Table 4). Since the little group along this direction has lesser symmetry than C_{2v} , degeneracy is not enforced. This is shown by the spin-splitting along ΓZ in the zoomed insets *iv, v* of Fig. 4a. This is also true for the bands calculated along various other high symmetry directions (Supplementary Fig. 23), where the insets show degeneracy along ΓX and splitting along the other directions. In the ΓZ direction no bands are found to cross the E_F , and this is corroborated by ARPES as well as EBS. A hybridization related gap is observed with bands 13 and 14 being

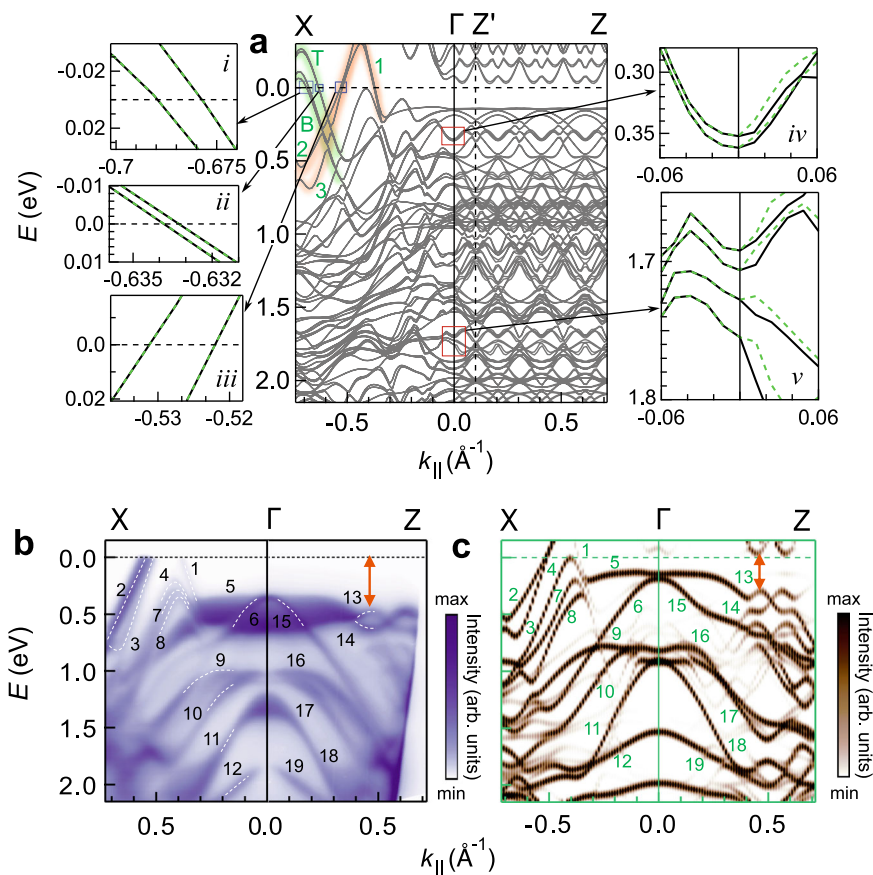


Fig. 4 | DFT and ARPES along and perpendicular to the KNL. a The band structure of LaTe₃ in the CDW state with the 7f structure along XT'Z'Z. On the left, zoomed regions from the blue rectangles show the two fold degeneracy (dashed-green and black) of the bands along the KNL. On the right, zoomed regions from the red rectangles show the spin-splitting along the Γ Z direction in contrast to Γ X. The

bands that cross E_F are highlighted by orange and green shading. **b** ARPES intensity plot measured using photon energy of 24.4 eV, and **c** the EBS obtained from DFT towards Γ X and Γ Z. The white dashed curves in **b** serve as guide to the eye for some of the bands that are numbered from 1 to 19. The orange double sided arrows indicate the CDW gap. All the panels share the same x axis.

the highest occupied ones (orange double arrow in Fig. 4b, c). This gap has been referred to as the CDW gap in LaTe₃³⁶ and other RTe₃ systems^{45,49,50,62,64}. A discussion about the variation of the CDW gap of LaTe₃ with k_x and k_y is provided in the Supplementary Note 5.

Discussion

As discussed in the previous section, DFT calculations for the 7f structure have demonstrated the existence of the nodal lines. In addition, an outstanding overall agreement with ARPES is obtained, which can be related to the small difference of the atom positions compared to x-ray crystallography (see Supplementary Fig. 2b). Nevertheless, it is crucial to establish the nodal lines for the 29f structure of LaTe₃, whose atom positions are indistinguishable from x-ray crystallography³³ within the experimental accuracy, as shown in Supplementary Fig. 2a.

Here, the results of our DFT calculations with SOC for the 29f structure at $k_x = 0.59 \text{ \AA}^{-1}$ in Fig. 5a, b show that the KNL related crossings at T and B are intact, and their dispersion around the crossings is quadratic, as in the 7f structure. The crossings appear at 0.197 \AA^{-1} that is slightly different from 7f (0.204 \AA^{-1}) because the size of their BZs are not integral multiple of each other (BZ of 29f is $\frac{7}{29}$ times reduced along k_z). To show the nodal line character of the KNL, we show these crossings at another k_x value of 0.685 \AA^{-1} in Supplementary Fig. 24a, b.

The KNL indicated by these crossings appears along the Σ line. The spin degeneracy of the bands along Γ X confirms this, whereas, in contrast, the degeneracy is lifted along Γ Z. This is shown in Fig. 5e, f which are zoomed regions enclosed by red rectangles in

Supplementary Fig. 25, where zoomed regions from the blue rectangles show this for other E ranges. Thus, the existence of the KNL is demonstrated for the CDW state of LaTe₃ with the 29f structure. Its behavior is similar to that of the 7f structure since both possess the same symmetry.

DFT calculations w/o SOC for the 29f structure show the existence of the spinless nodal lines related to the L and R crossings (see Fig. 5g, h for $k_x = 0.59 \text{ \AA}^{-1}$ and Supplementary Fig. 24c, d for $k_x = 0.685 \text{ \AA}^{-1}$), as in the 7f structure. These spinless nodal lines comprise of crossings of nondegenerate bands with distinct irreps that are linear and traverse the E_F with high Fermi velocity. These are however gapped out with SOC (Fig. 5c, d). This behavior resembles non-centrosymmetric topological nodal line semimetals such as pinictides e.g., CaAgAs, where the SOC-induced gap results in a topological insulator phase^{65,66}. Whether the SOC-induced gap in LaTe₃ has a topological character is an open question that would require further research.

The appearance of two distinct types of nodal lines (spinless and KNL) discussed above can be attributed to the bilayer splitting, that splits both the shadow and the main bands belonging to different irreps. The crossings of the CDW-induced shadow with the main bands are enforced by the KNL. The crossings occur from $E \sim 0.6 \text{ eV}$ and disperse in E to traverse the E_F as k_x increases (Fig. 3n). This dispersion in E is related to the dispersion of the main band (the crossing of the main band with E_F moves to larger k_z as k_x decreases, see Fig. 2a–d, h–k) coupled with the constraint that the shadow band is separated from it by \mathbf{q}_{CDW} . Other spin degenerate bands also cross the E_F along the KNL. So, we characterize LaTe₃ to be a KNL metal in

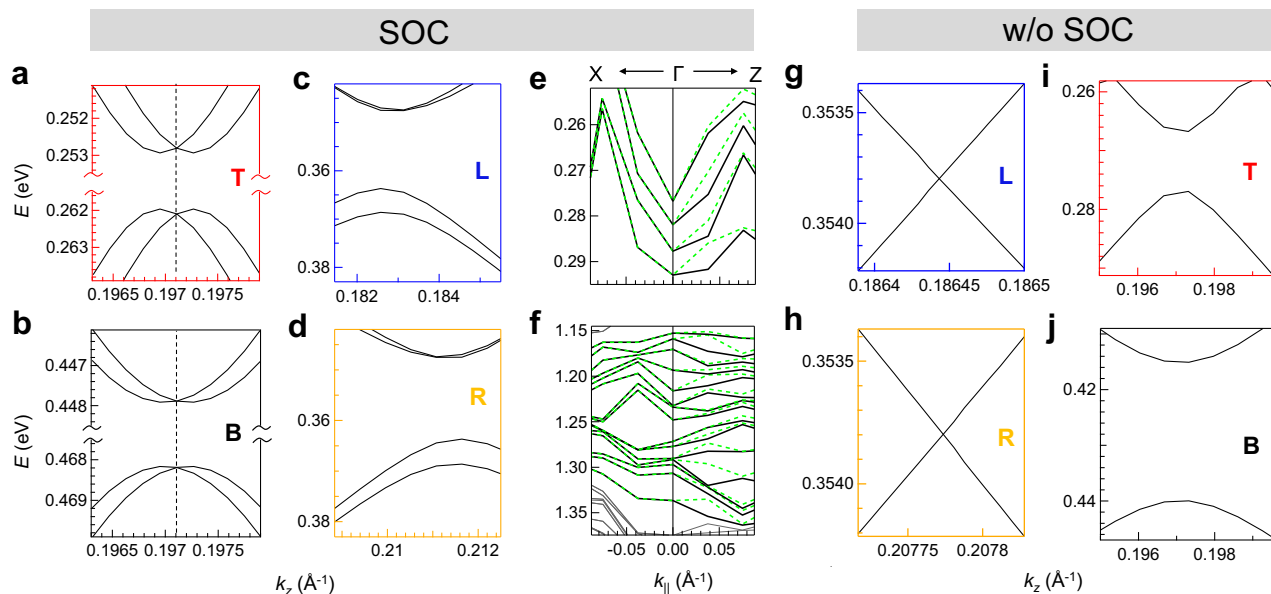


Fig. 5 | Band crossings for 29 fold LaTe₃ at $k_x = 0.59 \text{ \AA}^{-1}$. Band dispersion with SOC around **a** T, **b** B, **c** L, and **d** R. **e**, **f** Two fold degenerate bands (dashed-green and black) along TX and splitting along TZ shown in magnified scale. Band dispersion w/o SOC around **g** L, **h** R, **i** T, and **j** B.

the CDW state based on multiple bands crossing the E_F both along and perpendicular to the nodal line.

In conclusion, the identification of the shadow band from both ARPES and DFT is the foundation of our study. Its interaction with main band—studied using DFT for an incommensurate system with a realistic structure within experimental accuracy—resulted in the revelation of CDW-induced KNL in LaTe₃, a non-centrosymmetric, quasi-2D, TRS-preserving incommensurate material. This discovery is the cornerstone of our investigation, which we believe will inspire further research in the fascinating field of CDW materials.

Methods

Experimental

Single crystals of LaTe₃ with residual resistivity ratio [$\rho(300 \text{ K})/\rho(2 \text{ K})$] of ~ 270 ³⁰ were grown by tellurium flux technique, where high-purity La and Te were mixed in a molar ratio of La_{0.025}Te_{0.975}. This mixture was sealed under high vacuum in a crucible and heated at 900 °C for 10 h, and subsequently cooled slowly to 600 °C in 4 days. Excess Te was separated using a high-temperature centrifuge, resulting in gold-colored, plate-like LaTe₃ crystals. The ARPES measurements presented here were performed at the SGM3 beamline at the ASTRID2 synchrotron facility⁶⁷. ARPES data at SGM3 beamline were collected with an energy resolution of 18 meV at $h\nu = 24.4 \text{ eV}$. The angular resolution was 0.2° (0.008 Å⁻¹). The measurements were performed at 100 K with different photon energies ranging from 13 to 140 eV. Linearly polarized photon beam in the horizontal plane was incident at an angle of 50° with respect to the surface normal oriented along the analyzer axis. The analyzer slit is oriented vertically, and thus the detection plane is vertical. The polarization vector of the incident photon beam thus has two components parallel (*p* polarization) and perpendicular (*s* polarization) to the detection plane. The ARPES geometry is shown in Supplementary Fig. 26. All the measurements were done on freshly cleaved surfaces at a chamber base pressure better than 2×10^{-10} mbar. The ARPES intensity plots measured as a function of photon energy (*hν*) have been converted to k_y assuming the free electron final states⁶⁸. The raw data (E_{kin} vs $h\nu$) have been converted to E vs k_y by utilizing the expression $k_y = \frac{1}{\hbar} \sqrt{2m(E_{kin} \cos^2 \theta + V_0)}$, where E_{kin} is the kinetic energy of the photoelectrons, θ is the emission angle and the inner potential V_0 has been assumed to be 7.5 eV based on the best matching with the ARPES data.

The curvature plots have been obtained as in our earlier work^{69,70} with respect to both E and k axes following the method proposed by Zhang et al.⁷¹. This method improves the visibility of the weaker bands in the ARPES intensity plots and is better than the second derivative approach. The data analysis has been performed using IGOR pro (version 9). The dashed curves in Fig. 2e, f are obtained by a curve fitting the maxima of the MDCs. The maxima are identified by fitting the MDCs with Lorentzian functions. The least-square error method has been used for the curve fitting. The momentum resolution of ARPES represents the error in determining \mathbf{q}_{CDW} .

The STM measurements were carried out at a base pressure of 2×10^{-11} mbar using a variable temperature STM from Omicron Nanotechnology GmbH, while LEED and preliminary ARPES measurements were carried out in a workstation from Prevac sp. z o.o. STM was performed in the constant current mode using a tungsten tip that was cleaned by sputtering and voltage pulse method. The tip was biased and sample was kept at the ground potential. LEED is performed using a four grid rear view optics from OCI Vacuum Microengineering. Both STM and LEED were performed in the CDW state at room temperature. The error in the \mathbf{q}_{CDW} value from STM has been determined from the inverse of the step size of the topography image. In case of LEED, the error was determined from the pixel width of the pattern.

Density functional theory. The DFT calculations have been performed for the 7f and 29f structures of LaTe₃ with $C2cm$ space group ($SG \#40$). These structures have been derived from the experimental atomic positions at 100 K reported in ref. 33 using the PSEUDO program. The PSEUDO program⁷² displaces the atoms to arrive at the 7f and 29f structures with $C2cm$ space group. The structure file for 29f LaTe₃ (Supplementary Data 1) is provided in the Supplementary Information. VESTA software has been used for Crystal structure visualization⁷³.

We have employed the DFT-based Vienna Ab-initio Simulation Package (VASP)^{74,75} within the framework of the projector augmented wave method (PAW)^{74,75} to investigate the electronic structure of LaTe₃. The exchange-correlation functional is treated under the generalized gradient approximation (GGA) given by Perdew, Burke, and Ernzerhof⁷⁶. We have considered 11 valence electrons of the La atom ($5s^2 5p^6 5d^4 6s^2$) and 6 valence electrons of Te atom ($5s^2 5p^4$) in the PAW pseudopotential. The energy cut-off is set to 500 eV for the expansion of the planewaves. The convergence criterion for energy in the self-

consistent-field cycle and total force tolerance on each atom are taken to be 10^{-6} eV and 0.02 eV/Å, respectively. The SOC is employed by a second-variation method as implemented in the VASP code⁷⁵. To calculate the EBS, we have unfolded the band structure of the CDW state into the primitive BZ of the non-CDW state, using the PyProcar python code⁵⁸. All the DFT bands (and consequently the EBS) are rigidly shifted to larger E by 0.1 eV with respect to the E_F for comparison with the ARPES data.

The VASP calculations were carried out with the experiment-based 7f and 29f structures without geometry optimization. This approach has been used in the literature for complicated structures with a large unit cell, especially with modulation or anti-site defects^{27,77–80}. Nevertheless, our calculation with full geometry optimization including the van der Waals interaction by the DFT-D3 method (the electron-phonon interaction was not considered) retains the CDW state with q_{CDW} practically unchanged. But, the CDW amplitude decreases drastically by 80% compared to the experimental value from x-ray crystallography. Also, the CDW gap along ΓZ is not obtained, as shown in Supplementary Fig. 27a. The EBS calculation shows that the spectral weight of the shadow bands is much lower and so these are virtually non-existent (Supplementary Fig. 27b). These results are in stark disagreement with ARPES and justifies the use of the experiment-based structure without optimization for performing the DFT calculations.

In order to reconfirm the band crossings and to identify their irreps, DFT calculations have been performed using the all-electron WIEN2k programme package⁸¹ and Quantum Espresso software package⁸². Supplementary Fig. 28 shows that the bands are in agreement between VASP and WIEN2k. The latter was performed with energy cut-off of 16 Ry, where the $R_{MT}K_{max}$ value is taken to be 9.5. Further, we have used 10 for the maximum value of angular momentum for the (l,m) expansion of wave function or density. Convergence criteria for energy and charge have been taken to be 10^{-5} Ry and $0.001 e^-$, respectively. Quantum Espresso calculations have been carried out using fully relativistic PAW pseudopotentials for La and Te atoms. A planewave cutoff of 80 Ry and a $6 \times 6 \times 1$ k-grid were taken along with the energy accuracy of 10^{-8} Ry.

Data availability

The data that support the findings of this study are available from the corresponding authors upon request.

References

- Wang, Y. et al. Axial Higgs mode detected by quantum pathway interference in RTe_3 . *Nature* **606**, 896 (2022).
- Jiang, Y.-X. et al. Unconventional chiral charge order in kagome superconductor KV_3Sb_5 . *Nat. Mater.* **20**, 1353 (2021).
- Shi, W. et al. A charge-density-wave topological semimetal. *Nat. Phys.* **17**, 381 (2021).
- Rettig, L. et al. Persistent order due to transiently enhanced nesting in an electronically excited charge density wave. *Nat. Commun.* **7**, 10459 (2016).
- Luo, H. et al. Electronic nature of charge density wave and electron-phonon coupling in kagome superconductor KV_3Sb_5 . *Nat. Commun.* **13**, 273 (2022).
- Yu, F. H. et al. Unusual competition of superconductivity and charge-density-wave state in a compressed topological kagome metal. *Nat. Commun.* **12**, 3645 (2021).
- Zong, A. et al. Evidence for topological defects in a photoinduced phase transition. *Nat. Phys.* **15**, 27 (2018).
- Li, H. et al. Observation of unconventional charge density wave without acoustic phonon anomaly in kagome superconductors AV_3Sb_5 ($A = Rb, Cs$). *Phys. Rev. B* **11**, 031050 (2021).
- Song, Z. et al. Observation of an incommensurate charge density wave in monolayer $TiSe_2/CuSe/Cu(111)$ heterostructure. *Phys. Rev. Lett.* **128**, 026401 (2022).
- Lv, B. Q. et al. Unconventional hysteretic transition in a charge density wave. *Phys. Rev. Lett.* **128**, 036401 (2022).
- Pan, H., Xie, M., Wu, F. & Das Sarma, S. Topological phases in AB-stacked $MoTe_2/WSe_2$: Z_2 topological insulators, chern insulators, and topological charge density waves. *Phys. Rev. Lett.* **129**, 056804 (2022).
- D'Souza, S. W. et al. Coexistence of charge-density wave and ferromagnetism in Ni_2MnGa . *Phys. Rev. B* **85**, 085123 (2012).
- Gooth, J. et al. Axionic charge-density wave in the Weyl semimetal $(TaSe_4)_2I$. *Nature* **575**, 315 (2019).
- Qian, X., Liu, J., Fu, L. & Li, J. Quantum spin hall effect in two-dimensional transition metal dichalcogenides. *Science* **346**, 1344 (2014).
- Polshyn, H. et al. Topological charge density waves at half-integer filling of a moiré superlattice. *Nat. Phys.* **18**, 42 (2021).
- Mitsuishi, N. et al. Switching of band inversion and topological surface states by charge density wave. *Nat. Commun.* **11**, 2466 (2020).
- Lei, S. et al. Band engineering of Dirac semimetals using charge density waves. *Adv. Mater.* **33**, 2101591 (2021).
- Hsu, M.-C. et al. Topological theory of inversion-breaking charge-density-wave monolayer 1T- $TiSe_2$. *N. J. Phys.* **23**, 093025 (2021).
- Bzdušek, T., Wu, Q., Rüegg, A., Sigrist, M. & Soluyanov, A. A. Nodal-chain metals. *Nature* **538**, 75 (2016).
- Xia, Y., Cai, X. & Li, G. Multitype Dirac fermions protected by orthogonal glide symmetries in a non-centrosymmetric system. *Phys. Rev. B* **102**, 041201 (2020).
- Gao, H. et al. Dirac-Weyl semimetal: Coexistence of Dirac and Weyl fermions in polar hexagonal ABC crystals. *Phys. Rev. Lett.* **121**, 106404 (2018).
- Oh, Y.-T., Min, H.-G. & Kim, Y. Dual topological nodal line and nonsymmorphic Dirac semimetal in three dimensions. *Phys. Rev. B* **99**, 201110 (2019).
- Leonhardt, A. et al. Symmetry-enforced topological band crossings in orthorhombic crystals: classification and materials discovery. *Phys. Rev. Mater.* **5**, 124202 (2021).
- Chang, G. et al. Topological quantum properties of chiral crystals. *Nat. Mater.* **17**, 978 (2018).
- Xie, Y.-M. et al. Kramers nodal line metals. *Nat. Commun.* **12**, 3064 (2021).
- Yu, R., Weng, H., Fang, Z., Dai, X. & Hu, X. Topological node-line semimetal and Dirac semimetal state in antiperovskite Cu_3PdN . *Phys. Rev. Lett.* **115**, 036807 (2015).
- Shang, T. et al. Unconventional superconductivity in topological Kramers nodal-line semimetals. *Sci. Adv.* **8**, eabq6589 (2022).
- Kogar, A. et al. Light-induced charge density wave in $LaTe_3$. *Nat. Phys.* **16**, 159 (2019).
- Zong, A. et al. Role of equilibrium fluctuations in light-induced order. *Phys. Rev. Lett.* **127**, 227401 (2021).
- Pariari, A. et al. Interplay between charge density wave order and magnetic field in the nonmagnetic rare-earth tritelluride $LaTe_3$. *Phys. Rev. B* **104**, 155147 (2021).
- Hu, B. F., Cheng, B., Yuan, R. H., Dong, T. & Wang, N. L. Coexistence and competition of multiple charge-density-wave orders in rare-earth tritellurides. *Phys. Rev. B* **90**, 085105 (2014).
- Yumigeta, K. et al. Advances in rare-earth tritelluride quantum materials: Structure, properties, and synthesis. *Adv. Sci.* **8**, 2004762 (2021).
- Malliakas, C. D. & Kanatzidis, M. G. Divergence in the behavior of the charge density wave in $RETe_3$ ($RE =$ rare-earth element) with temperature and RE element. *J. Am. Chem. Soc.* **128**, 12612 (2006).

34. Lavagnini, M. et al. Evidence for coupling between charge density waves and phonons in two-dimensional rare-earth tritellurides. *Phys. Rev. B* **78**, 201101 (2008).
35. Singha, R., Pariari, A. K., Satpati, B. & Mandal, P. Large nonsaturating magnetoresistance and signature of nondegenerate Dirac nodes in ZrSiS. *Proc. Natl Acad. Sci.* **114**, 2468 (2017).
36. Brouet, V. et al. Angle-resolved photoemission study of the evolution of band structure and charge density wave properties in RTe₃ (R=Y, La, Ce, Sm, Gd, Tb, and Dy). *Phys. Rev. B* **77**, 235104 (2008).
37. Hong, Y., Wei, Q., Liang, X. & Lu, W. Origin and strain tuning of charge density wave in LaTe₃. *Phys. B: Condens. Matter* **639**, 413988 (2022).
38. Johannes, M. D. & Mazin, I. I. Fermi surface nesting and the origin of charge density waves in metals. *Phys. Rev. B* **77**, 165135 (2008).
39. Eiter, H.-M. et al. Alternative route to charge density wave formation in multiband systems. *Proc. Natl Acad. Sci.* **110**, 64 (2012).
40. Janssen, T., Janner, A., Looijenga-Vos, A. and de Wolff, P. M. in <https://doi.org/10.1107/97809553602060000624> *International Tables for Crystallography* (International Union of Crystallography, 2006) pp. 907–955.
41. Van Smaalen, S. *Incommensurate crystallography*, Vol. 21 (Oxford University Press, 2007).
42. Dubois, J.-M. and Belin-Ferré, E. eds., <https://doi.org/10.1002/9783527632718> *Complex Metallic Alloys* (Wiley, 2010).
43. Sarkar, S. et al. Bulk electronic structure of high-order quaternary approximants. *Phys. Rev. Res.* **3**, 013151 (2021).
44. Singh, V. K. et al. Decagonal Sn clathrate on d-Al-Ni-Co. *Phys. Rev. B* **107**, 045410 (2023).
45. Komoda, H. et al. High-resolution angle-resolved photoemission study of incommensurate charge-density-wave compound CeTe₃. *Phys. Rev. B* **70**, 195101 (2004).
46. Mans, A. et al. Experimental proof of a structural origin for the shadow Fermi surface of Bi₂Sr₂CaCu₂O_{8+δ}. *Phys. Rev. Lett.* **96**, 107007 (2006).
47. DiMasi, E., Aronson, M. C., Mansfield, J. F., Foran, B. & Lee, S. Chemical pressure and charge-density waves in rare-earth tritellurides. *Phys. Rev. B* **52**, 14516 (1995).
48. Novoselov, K. S. et al. Two-dimensional gas of massless Dirac fermions in graphene. *Nature* **438**, 197 (2005).
49. Gweon, G.-H. et al. Direct observation of complete Fermi surface, imperfect nesting, and gap anisotropy in the high-temperature incommensurate charge-density-wave compound SmTe₃. *Phys. Rev. Lett.* **81**, 886 (1998).
50. Brouet, V. et al. Fermi surface reconstruction in the cdw state of CeTe₃ observed by photoemission. *Phys. Rev. Lett.* **93**, 126405 (2004).
51. Ohta, T., Bostwick, A., Seyller, T., Horn, K. & Rotenberg, E. Controlling the electronic structure of bilayer graphene. *Science* **313**, 951 (2006).
52. Feng, D. L. et al. Bilayer splitting in the electronic structure of heavily overdoped Bi₂Sr₂CaCu₂O_{8+δ}. *Phys. Rev. Lett.* **86**, 5550 (2001).
53. Garcia, D. R. et al. Revealing charge density wave formation in the LaTe₂ system by angle resolved photoemission spectroscopy. *Phys. Rev. Lett.* **98**, 166403 (2007).
54. Shin, K. Y., Brouet, V., Ru, N., Shen, Z. X. & Fisher, I. R. Electronic structure and charge-density wave formation in LaTe_{1.95} and CeTe_{2.00}. *Phys. Rev. B* **72**, 085132 (2005).
55. Yang, B.-J. & Kee, H.-Y. Searching for topological density-wave insulators in multiorbital square-lattice systems. *Phys. Rev. B* **82**, 195126 (2010).
56. Ku, W., Berlijn, T. & Lee, C.-C. Unfolding first-principles band structures. *Phys. Rev. Lett.* **104**, 216401 (2010).
57. Popescu, V. & Zunger, A. Effective band structure of random alloys. *Phys. Rev. Lett.* **104**, 236403 (2010).
58. Herath, U. et al. PyProcar: a python library for electronic structure pre/post-processing. *Computer Phys. Commun.* **251**, 107080 (2020).
59. Bader, R. F. Atoms in molecules. *Acc. Chem. Res.* **18**, 9 (1985).
60. Bhattacharya, J. & Chakrabarti, A. Electronic and transport properties of heusler alloy based magnetic tunneling junctions: A first principles study. *Computational Mater. Sci.* **216**, 111852 (2023).
61. Sarkar, S. et al. X-ray photoelectron spectroscopy study of a layered tri-chalcogenide system LaTe₃. *AIP Conf. Proc.* **2220**, 100005 (2020).
62. Chikina, A. et al. Charge density wave generated Fermi surfaces in NdTe₃. *Phys. Rev. B* **107**, L161103 (2023).
63. Elcoro, L. et al. Double crystallographic groups and their representations on the Bilbao crystallographic server. *J. Appl. Crystallogr.* **50**, 1457 (2017).
64. Lee, E. et al. The 7 × 1 Fermi surface reconstruction in a two-dimensional *f*-electron charge density wave system: PrTe₃. *Sci. Rep.* **6**, 30318 (2016).
65. Yamakage, A., Yamakawa, Y., Tanaka, Y. & Okamoto, Y. Line-node Dirac semimetal and topological insulating phase in non-centrosymmetric pnictides CaAgX(X = P, As). *J. Phys. Soc. Jpn* **85**, 013708 (2016).
66. Lv, B. Q., Qian, T. & Ding, H. Experimental perspective on three-dimensional topological semimetals. *Rev. Mod. Phys.* **93**, 025002 (2021).
67. Hoffmann, S., Søndergaard, C., Schultz, C., Li, Z. & Hofmann, P. An undulator-based spherical grating monochromator beamline for angle-resolved photoemission spectroscopy. *Nucl. Instrum.* **523**, 441 (2004).
68. Ngankeu, A. S. et al. Quasi-one-dimensional metallic band dispersion in the commensurate charge density wave of 1T-TaS₂. *Phys. Rev. B* **96**, 195147 (2017).
69. Singha, R. et al. Signatures of topological surface state and unconventional magnetotransport properties in elemental Ruthenium. *Adv. Quantum Technol.* **6**, 2200116 (2023).
70. Sadhukhan, P. et al. Electronic structure of Au-Sn compounds grown on Au(111). *Phys. Rev. B* **100**, 235404 (2019).
71. Zhang, P. et al. A precise method for visualizing dispersive features in image plots. *Rev. Sci. Instrum.* **82**, 043712 (2011).
72. Capillas, C. et al. A new computer tool at the Bilbao crystallographic server to detect and characterize pseudosymmetry. *Z. für Kristallographie* **226**, 186 (2011).
73. Momma, K. & Izumi, F. Vesta 3 for three-dimensional visualization of crystal, volumetric and morphology data. *J. Appl. Crystallogr.* **44**, 1272 (2011).
74. Kresse, G. & Furthmüller, J. Efficient iterative schemes for *ab-initio* total-energy calculations using a plane-wave basis set. *Phys. Rev. B* **54**, 11169 (1996).
75. Kresse, G. & Joubert, D. From ultrasoft pseudopotentials to the projector augmented-wave method. *Phys. Rev. B* **59**, 1758 (1999).
76. Perdew, J. P., Burke, K. & Ernzerhof, M. Generalized gradient approximation made simple. *Phys. Rev. Lett.* **77**, 3865 (1996).
77. Razzoli, E. et al. Stable Weyl points, trivial surface states, and particle-hole compensation in WP₂. *Phys. Rev. B* **97**, 201103 (2018).
78. Singh, S. et al. Spin-valve-like magnetoresistance in Mn₂NiGa at room temperature. *Phys. Rev. Lett.* **109**, 246601 (2012).
79. Bhattacharya, J. et al. Bulk electronic structure of Ni₂MnGa studied by density functional theory and hard x-ray photoelectron spectroscopy. <https://arxiv.org/abs/2304.04992> preprint at <https://arxiv.org/abs/2304.04992> (2023).
80. Pinek, D. et al. Unified description of the electronic structure of M₂AC nanolamellar carbides. *Phys. Rev. B* **100**, 075144 (2019).
81. Blaha, P. et al. WIEN2k: An augmented plane wave plus local orbitals program for calculating crystal properties. *Techn. Universität* **60** (2001)

82. Baroni, S., de Gironcoli, S., Dal Corso, A. & Giannozzi, P. Phonons and related crystal properties from density-functional perturbation theory. *Rev. Mod. Phys.* **73**, 515 (2001).
83. Setyawan, W. & Curtarolo, S. High-throughput electronic band structure calculations: challenges and tools. *Comput. Mater. Sci.* **49**, 299 (2010).

Acknowledgements

S.S., P.S., and S.R.B. gratefully acknowledge the financial support from the Department of Science and Technology, Government of India within the framework of the DST-Synchrotron-Neutron Project to perform experiments at ASTRID2 synchrotron facility. A part of this work was supported by VILLUM FONDEN via the Centre of Excellence for Dirac Materials (Grant No. 11744). Anushree Roy is thanked for providing the Raman data. The Computer division of Raja Ramanna Centre for Advanced Technology is thanked for installing the DFT codes and providing support throughout.

Author contributions

S.S., P.S., D.C., and S.R.B. conducted the ARPES measurements with assistance and support from M.B. and P.H. LEED was carried out by S.S. and P.S., while STM was performed by V.K.S. J.B. and R.D. did the DFT calculations under the supervision of A.C. The explanation of the results was provided by S.S., T.D., A.C., and S.R.B. The single crystals of LaTe_3 were grown by A.P., S.R., and P.M., the latter introduced us to this system. S.S. analyzed the experimental data with initial help from D.C., performed the post-analysis of the DFT results with some inputs from J.B., and prepared the figures. The project was planned and led by S.R.B. who wrote the paper with significant contributions from S.S., P.H., and A.C.

Competing interests

The authors declare no competing interests.

Additional information

Supplementary information The online version contains supplementary material available at <https://doi.org/10.1038/s41467-023-39271-1>.

Correspondence and requests for materials should be addressed to Sudipta Roy Barman.

Peer review information *Nature Communications* thanks the anonymous reviewers for their contribution to the peer review of this work. A peer review file is available.

Reprints and permissions information is available at <http://www.nature.com/reprints>

Publisher's note Springer Nature remains neutral with regard to jurisdictional claims in published maps and institutional affiliations.

Open Access This article is licensed under a Creative Commons Attribution 4.0 International License, which permits use, sharing, adaptation, distribution and reproduction in any medium or format, as long as you give appropriate credit to the original author(s) and the source, provide a link to the Creative Commons license, and indicate if changes were made. The images or other third party material in this article are included in the article's Creative Commons license, unless indicated otherwise in a credit line to the material. If material is not included in the article's Creative Commons license and your intended use is not permitted by statutory regulation or exceeds the permitted use, you will need to obtain permission directly from the copyright holder. To view a copy of this license, visit <http://creativecommons.org/licenses/by/4.0/>.

© The Author(s) 2023